ACS APPLIED MATERIALS & INTERFACES

www.acsami.org

Forum Article

"Invisible" Digital Light Processing 3D Printing with Near Infrared Light

Lynn M. Stevens, Clotilde Tagnon, and Zachariah A. Page*

Cite This: https://doi.org/10.1021/acsami.1c22046

Read Online

ACCESS | Metrics & More | Article Recommendations | Supporting Information

ABSTRACT: The ability to 3D print structures with low-intensity, long-wavelength light will broaden the materials scope to facilitate inclusion of biological components and nanoparticles. Current materials limitations arise from the pervasive absorption, scattering, and/or degradation that occurs upon exposure to high-intensity, short-wavelength (ultraviolet) light, which is the present-day standard used in light-based 3D printers. State-of-the-art techniques have recently extended printability to orange/red light. However, as the wavelength of light increases, so do the inherent challenges to match the speed and resolution of traditional UV light-induced solidification processes (i.e., photocuring). Herein, a photosystem is demonstrated to enable low-intensity (<5 mW/cm^2), long-wavelength (~850 nm) near-infrared (NIR) light-driven 3D printing, "invisible" to the human eye. The combination of a NIR absorbing cyanine dye with electron-rich and -deficient redox pairs was required for rapid photocuring in a catalytic manner. The rate of polymerization and time to solidification upon exposure to NIR light were characterized via in situ spectroscopic and rheological monitoring. Translation to NIR digital light processing (projection-based) 3D printing was accomplished through rigorous optimization of resin composition and printing parameters to balance the speed (<60 s/layer) and resolution (<300 μm features). As a proof-of-concept, composite 3D printing with nanoparticle-infused resins was accomplished. Preliminary analysis showed improved feature fidelity for structures produced with NIR relative to UV light. The present report provides key insight that will inform next-generation light-based photocuring technology, such as wavelength-selective multimaterial 3D bio- and composite-printing.

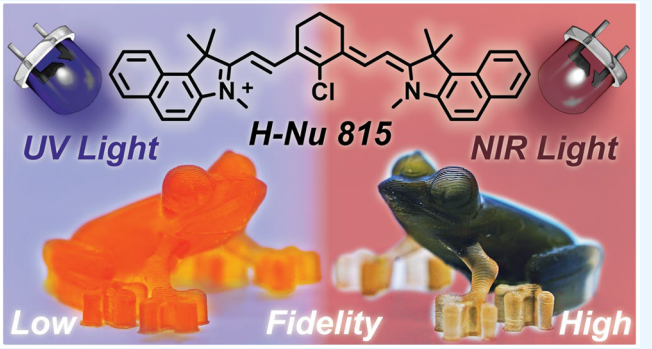

KEYWORDS: *3D printing, digital light processing, near infrared light, nanocomposites, cyanine dyes*

INTRODUCTION

Additive manufacturing (3D printing) technology has experienced tremendous growth in recent years because of its increased manufacturing speed, high feature resolution, little waste, and low equipment cost relative to traditional "subtractive" processes.[1−6] Vat photopolymerization 3D printing, which relies on light to rapidly convert liquid resins into solid objects (photocuring), has gained considerable attention. Contemporary light-based 3D printing methods include digital light processing (DLP) and liquid crystal display (LCD) printing, where each layer is photocured with spatiotemporal control by a sequence of 2D image projections. Both DLP and LCD offer unmatched combinations of speed (<5 s/layer) and feature resolution (<100 μm) at affordable prices (starting at $150) and manageable printer footprints (suitable for most tabletops).[7] Despite these positive attributes, the reliance on ultraviolet (UV) and violet light (wavelength, $\lambda \lesssim 405$ nm) activated chemistry limits the scope of accessible materials via photopolymerization.[1,8]

Printing with UV−violet light has led to many impressive discoveries, such as continuous liquid interface production[9] and high area rapid printing.[10] However, expanding printability to include milder visible ($\lambda \approx 400-780$ nm) and near-infrared (NIR, $\lambda \geq 780$ nm) light would enable the use of UV-intolerant materials.[11−14] Specifically, this would allow for production of resins that significantly attenuate UV−violet light via absorption and/or scattering. These might include resins that contain cells (bioprinting)[15,16] and nanoparticles (composite printing).[14] Diversifying printable materials will provide access to advanced objects with applications in regenerative medicine, aerospace, and beyond.

Recently, our research group reported a chemical strategy to enable DLP 3D printing with visible-to-far-red light ($\lambda \approx 470-620$ nm; intensity, $I \approx 2-3$ mW/cm^2) at build speeds (33−45 mm/h) and resolutions (<100 μm lateral and 25 μm vertical

Special Issue: Early Career Forum

Received: November 13, 2021
Accepted: January 17, 2022

features) competitive with contemporary UV-based systems.[17−19] Rapid photocuring (≲60 s) was enabled by multicomponent photosystems that operated via a Type II reaction mechanism. In general, Type II photocuring requires two or three components: an absorbing dye molecule paired with a donor and/or acceptor co-initiator molecule. Type II photocuring has also facilitated recent visible-light 3D printing by Hawker, Valentine, and co-workers with a visible LED projector ($\lambda \approx 470-550$ nm) to prepare polymer foams,[20] from Zhao, Xu, and co-workers with a blue laser projector ($\lambda \approx 445$ nm, $I \approx 10$ mW/cm^2) to prepare recyclable polymers,[21] and from Boyer, Corrigan, and co-workers with a green LED projector ($\lambda \approx 525$ nm, $I \approx 0.3$ mW/cm^2) to prepare 4D hydrogel actuators.[22] Additionally, visible-light DLP[23] and LCD[24] projection from smartphones have recently been reported for 3D printing. 3D printing with NIR light has also been accomplished, but with caveats of complex and expensive setups reliant on high powered lasers (>1 W/cm^2)[25,26] that are orders of magnitude more intense than what DLP and LCD printers typically output (∼1−40 mW/cm^2). Thus, opportunities to advance light-induced projection-based 3D printing include (1) photocuring at wavelengths >620 nm and (2) leveraging longer wavelengths of light for bio- or composite-printing.

Photocuring with NIR light typically follows the same Type II mechanism mentioned previously for visible-light systems.[27−29] Inducing rapid photocuring requires strong dye absorption and efficient electron transfer to/from a co-initiator. A common strategy to red shift absorption has been to increase π-conjugation, whereas the electron transfer efficiency has been improved by increasing the excited-state lifetime.[18] However, these two strategies are often at odds, as explained by the energy gap law,[30,31] which notes that decreasing the energy gap by increasing π-conjugation results in shorter excited-state lifetimes. Thus, efficient NIR photocuring is an ongoing challenge. State-of-the-art examples include those from Strehmel and co-workers[32−35] as well as Lalevée and co-workers,[36−38] primarily using cyanine derivatives as the NIR light absorbers. However, NIR light intensities (∼0.4−4 W/cm^2) that are impractical for DLP or LCD printing were required for accessing rapid polymerization (≲60 s) in these studies.

The fabrication of composites, in which nanomaterials are incorporated into polymer networks to prepare objects with improved mechanical, optical, and/or thermal properties, is relevant to NIR photocuring. Currently, their rapid high-resolution printing has been hampered by the intrinsic attenuation of UV light via absorption and/or scattering.[14] Although absorption primarily influences curing along the z-direction, scattering can induce curing in all (x,y,z) directions, which decreases overall resolution. Within the Rayleigh scattering regime, the intensity of light scattering is proportional to the sixth power of the particle diameter and to the fourth power of the reciprocal wavelength of incident light.[39] Additionally, small changes in particle refractive index ($n_{particle}$) relative to the solvent ($n_{solvent}$) can result in large changes in scattering intensity (e.g., a change in $n_{particle}/n_{solvent}$ from 1.1 to 2.0 results in a ∼60× increase in scattering intensity).[40] Thus, decreasing the particle size, increasing the wavelength, and/or decreasing $n_{particle}/n_{solvent}$ are three methods to significantly reduce light scattering and improve the printing speed and resolution. Because the minimum particle size and size distribution are limited by the fabrication process and the refractive indices are intrinsic properties, increasing the wavelength of light is a compelling avenue to reduce light scattering without limiting the scope of accessible materials.

Herein, a novel NIR photosystem is described along with its use in low-intensity (4.6 mW/cm^2) DLP 3D printing with an ∼850 nm LED (Figure 1). Resin formulation optimization was

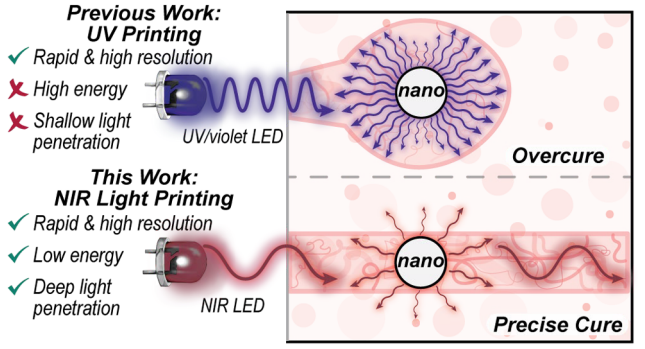

Figure 1. Effect of incident wavelength on scattering in light-based 3D printing. Contemporary digital light processing (DLP) 3D printing relies on ultraviolet (UV) light, which leads to shallow penetration and overcure from intense scattering. The present work describes near-infrared (NIR) light DLP, with deeper light penetration and more precise curing due to reduced scattering.

performed by monitoring polymerization kinetics using real time infrared spectroscopy and rheology during NIR irradiation. The 3D printing speed and resultant feature resolution were optimized by varying exposure time, layer thickness, and opaquing agent (carbon black) content. Additionally, NIR light-based composite printing was demonstrated using silica and zirconia nanoparticles. Lateral and vertical feature resolution of printed objects were characterized using optical profilometry to quantify the effect of light wavelength (405 vs 850 nm) and nanoparticle composition on printing fidelity.

RESULTS AND DISCUSSION

Initial experiments focused on identifying photosystem components to enable rapid polymerization (≲60 s) with NIR light. Following our research group's previous protocol that provided efficient visible-light photocuring,[17−19] a three-component photosystem comprising a photoredox catalyst along with donor and acceptor co-initiators was examined. When selecting a photoredox catalyst, cyanine 7 derivatives (those containing seven methine units) were desirable given their high molar absorptivity in the NIR region (≥100 000 M^{-1} cm^{-1}).[41] Specifically, a cyanine 7 derivative from Spectra Photopolymers called H-Nu 815 was selected given its precedent for NIR radiation curing used in coating applications[42] (Figure 2a). Notably, H-Nu 815 contains a butyltriphenylborate counteranion, which is known to be an efficient electron donor for photoexcited cyanines that results in the formation of a butyl radical initiator.[43,44] As such, a borate salt, specifically 2-(butyryloxy)-*N*,*N*,*N*-trimethylethan-1-aminium butyltriphenylborate (Borate V), was employed as the donor co-initiator. Post-photoinduced electron transfer, it was hypothesized that the reduced H-Nu 815 could be oxidized by a common diphenyliodonium salt to simultaneously regenerate H-Nu 815 to complete the catalytic cycle and produce additional initiating carbon-centered radicals to

https://doi.org/10.1021/acsami.1c22046
ACS Appl. Mater. Interfaces XXXX, XXX, XXX−XXX

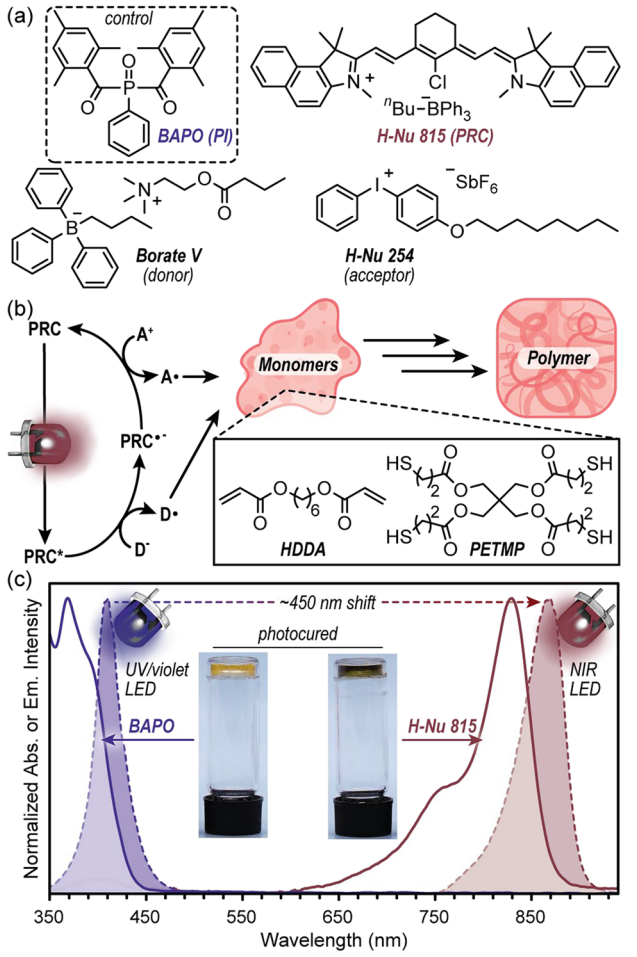

Figure 2. Resin composition, general mechanism, and absorption/emission profiles for UV−violet and NIR photocuring. (a) Chemical structures for NIR photosystem components that include H-Nu 815 as the photoredox catalyst (PRC), borate V as the electron donor (D), and H-Nu 254 as the electron acceptor (A), along with BAPO as a UV−violet light photoinitiator (PI) control. (b) Proposed general mechanism showing PRC to excited PRC (PRC*) upon absorption of light, followed by PRC reduction to $PRC^{\bullet-}$ by D and then oxidation back to PRC by A. Both D and A redox results in radical generation that initiates monomer to polymer conversion. Chemical structures of HDDA and PETMP monomers shown. (c) Normalized absorption profiles of BAPO and H-Nu 815 overlaid with UV−violet and NIR LED emission profiles. Inset images represent resin samples cured with 405 nm (left) and 850 nm (right) LEDs.

induce polymerization[45] (Figure 2b). Specifically, [4-(octyloxy)phenyl](phenyl)iodonium hexafluoroantimonate (H-Nu 254) was selected as the acceptor co-initiator. To compare results from the NIR light photosystem with contemporary Type I systems a photoinitiator (PI), bisacylphosphine oxide (BAPO), commonly utilized in 405 nm 3D printing, was employed as a control (Figure 2a).

The main resin constituents (monomers/cross-linkers) utilized in this study were 1,6-hexanediol diacrylate (HDDA) and pentaerythritol tetrakis(3-mercaptopropionate) (PETMP) (Figure 2b). This combination was selected to maximize the photopolymerization rate, as described below. In stark dichotomy to UV−violet LEDs that are centered at ∼365−405 nm in commercial 3D printers, the NIR LEDs used herein were centered at ∼850−870 nm (Figure 2c and Figure S3). This ∼450 nm red shift in LED output is shown in Figure 2c, along with the overlap each LED has with BAPO and H-Nu 815 absorption profiles. Quantitative extinction measurements of H-Nu 815 at resin conditions (0.1 mol % relative to a 95:5 molar ratio of HDDA:PETMP, ∼4.2 mM) were accomplished using UV−vis absorption spectroscopy by passing a probe light through the samples between glass slides with 25, 50, 75, and 100 μm spacers. The peak attenuation for H-Nu 815 was found at 829 nm with an extinction coefficient of 18 000 ± 3000 M^{-1} cm^{-1} (Figure S4). This value was lower than expected, given precedent for cyanines to have extinction coefficients in excess of 100 000 M^{-1} cm^{-1}.[41] The low extinction coupled with a raised baseline were both indicative of aggregation. As confirmation, *N*,*N*-dimethylacrylamide (DMA) was found to better solvate H-Nu 815, evident by an absorption baseline of ∼0 (Figure S5). Furthermore, the extinction coefficient of H-Nu 815 in DMA (0.02 mol %, ∼1.9 mM) was found to be ∼190 000 M^{-1} cm^{-1} at 829 nm. Qualitatively, the solubility of H-Nu 815 is low in most commercial acrylates used in 3D printing resins. As such, improving the solubility of the photoredox catalyst represents a potential future opportunity to further enhance photoreactivity. Despite the potential aggregation, the resin appeared to provide a stable suspension and was used going forward. As a qualitative test, photopolymer resins containing HDDA:PETMP (95:5) with either the BAPO photoinitiator or H-Nu 815 photosystem were found to rapidly cure (<60 s) upon exposure to the corresponding UV−violet or NIR LED at a printer intensity of 8.8 and 4.6 mW/cm^2, respectively (representative photocured samples are shown in the inset of Figure 2c).

The photocuring process was quantitatively characterized under ambient conditions (e.g., room temperature and in air) using real-time Fourier transform infrared spectroscopy (photoFTIR) to monitor monomer to polymer conversion (Figure 3a). Photorheology was performed in tandem with photoFTIR to determine the gel point, which is commensurate with a minimum exposure time required for DLP 3D printing. To mimic DLP 3D printing conditions, described in detail later, the sample thickness was set to 100 μm and NIR light intensity to 4.6 mW/cm^2 for all measurements. Using photoFTIR, conversion was determined by tracking the disappearance of C═C vinylic stretches at ∼3100 cm^{-1},[46] as well as the disappearance of the signal at ∼2570 cm^{-1} corresponding to the S−H stretch.[47] Initial experimentation focused on determining ideal concentrations for H-Nu 815 and the co-initiators to maximize the polymerization rate and minimize the material waste. In the absence of thiol (0% PETMP), no polymerization was observed within 2 min of irradiation, which is attributed to oxygen inhibition that influences Type II over Type I photosystems to a greater extent.[19] However, adding 1 mol % PETMP resulted in polymerization within 1 min of turning the light on and showed good temporal control with no notable dark polymerization (Figure S6). The optimal concentrations relative to bulk monomer (HDDA:PETMP, 99:1) were found to be 0.1 mol % (= 0.36 wt %) H-Nu 815, 0.1 mol % (= 0.4 wt %) Borate V, and 0.2 mol % (= 0.54 wt %) H-Nu 254 (optimization details found in section 3.2). Notably, these quantities are small in comparison to what is often used for Type I photoinitiators (∼1−5 wt %).[4] Under these conditions, the NIR photosystem provides an induction period of ∼14.7 ± 2.5 s (time from light on to the start of polymerization) with a maximum rate of 3.1 ± 0.3%/s (Table S3).

https://doi.org/10.1021/acsami.1c22046
ACS Appl. Mater. Interfaces XXXX, XXX, XXX−XXX

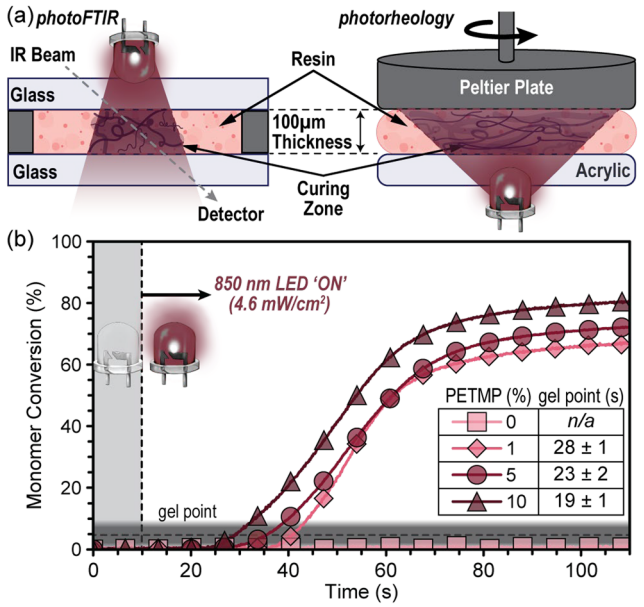

Figure 3. Photocuring characterization of NIR light reactive resins. (a) Schematic representations of the real-time Fourier transform infrared spectroscopy (photoFTIR) and photorheology setups. (b) PhotoFTIR results for resins comprising 0.1 mol % H-Nu 815, 0.1 mol % Borate V, and 0.2 mol % H-Nu 254 as the photosystem and varying amounts of PETMP in HDDA. The gel points acquired from photorheology experiments are represented by a gradient line that is underlaid on the conversion graph to show the similarly low conversion required for network formation. Average gel point times are provided in the inset table with ±1 standard deviation. For legibility, symbols present on the photoFTIR curves represent one in every 50 data points collected.

The effect of PETMP loading on induction period and polymerization rate was examined next. Testing 1, 5, and 10 mol % PETMP revealed that as PETMP was increased the polymerization rate remained largely unchanged, but the induction period decreased; 28.7 ± 2.1, 25.0 ± 3.0, and 16.3 ± 1.5 s, respectively (Table S4 and Figure S7). Higher values of PETMP (up to 33.3 mol % to match thiol to "ene" functionality) were examined but found to be too reactive, polymerizing within 45 min after preparation. Because of the high reactivity of these resins, inclusion of 2,2,6,6-tetramethyl-1-piperidinyloxy (TEMPO) as a radical inhibitor was necessary prior to 3D printing. Thus, 0.005 mol % and 0.01 mol % TEMPO were screened with 5 and 10 mol % PETMP, finding that 0.005 mol % TEMPO provided the best compromise between resin stability and induction period, 26.0 ± 2.7 and 16.7 ± 1.2 s, respectively (Figure 3b, Table S5, and Figure S9). With more PETMP, the slight increase in maximum monomer conversion is attributed to greater chain mobility. Gel points from photorheology were found to occur seconds from the induction periods observed with photoFTIR for 1, 5, and 10 mol % PETMP samples containing 0.005 mol % TEMPO; gel points = 28 ± 1, 23 ± 2, and 19 ± 1 s, respectively (Table S7 and Figures S11–S15). These gel points correspond to a monomer conversion of <10%, which is expected for a highly cross-linked system that operates via a free radical chain-growth mechanism. A 95:5 molar ratio of HDDA:PETMP was selected for future experiments. This resin composition was stable in the dark at room temperature for at least 12 h, which could be extended by separating out PETMP from the rest of the resin. Shelf life studies revealed that the resins without PETMP stored in a fridge (~2 °C) were stable for at least 2 weeks and had similar performance upon addition of PETMP prior to use (Table S8 and Figure S16).

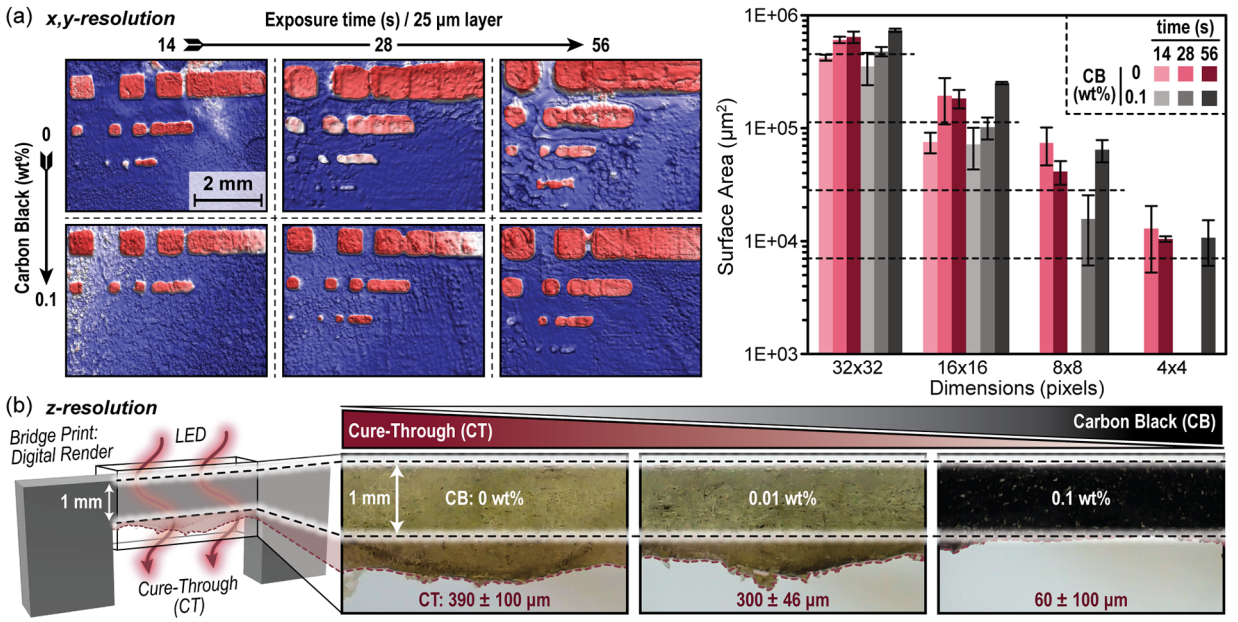

Figure 4. Optimization of NIR light 3D printing. (a) Optical profilometry images of square feature arrays printed with and without 0.1 wt % carbon black (CB) at different exposure times per 25 μm layer and corresponding surface area analysis to determine lateral (x,y) resolution. Dashed lines represent theoretical surface area and error bars represent ±1 standard deviation. (b) Digital rendering of bridge print file used to analyze vertical (z) resolution, and images of the bridge overhang in representative 3D prints. The CB content and average thickness ±1 standard is provided as an inset in each image. The dashed lines represent the target overhang z-height (1 mm).

https://doi.org/10.1021/acsami.1c22046
ACS Appl. Mater. Interfaces XXXX, XXX, XXX−XXX

After optimizing the resin formulation printing experiments ensued. Initially, the effect of exposure time per layer on resolution was determined qualitatively using custom digital files containing arrays of small square features from one pixel (= 21 μm) to 32 pixels (= 672 μm) wide (Figure S25). Imaging the resultant prints revealed that features were appearing at around 25 s for 100 μm thick layers, consistent with photoFTIR and photorheological data. However, curing outside of the irradiated zones (overcure) was evident, which was hypothesized to arise from a combination of light scattering and deep light penetration. Addition of opaquing agents was used to mitigate overcure. An azo-dye (Sudan I,[48] 0.04 wt %) was used as the opaquing agent for the UV−violet light control system. Carbon black (CB, 40 nm diameter) was selected as the opaquing agent for the NIR photosystem (Figures S17 and S22). For concentrations above 0.01 wt % CB (relative to monomer), stearic acid (0.4 wt %) and ultrasonication were required to provide a homogeneous and stable suspension. Notably, the presence of stearic acid reduced the induction period from 25.0 ± 3.0 s to 10.3 ± 1.2 s for NIR photopolymerizations, regardless of CB concentration (Table S9 and Figures S18 and S19). This rate enhancement was hypothesized to arise from a perturbation of H-Nu 815 aggregation in the presence of stearic acid, which is common for cyanine dyes[49,50] and is supported by changes in ground-state absorption (Figure S20). Despite light attenuation from CB, the presence of stearic acid enabled printing with exposure times of 14 s per 25 μm layer (Figure 4a and Figure S26). Optical profilometry was used to characterize the lateral resolution for different exposure times by measuring the top surface area of small squares in the arrays (Figure 4a and Figures S27−S29). Overall, the presence of carbon black provided reduced overcure, and longer exposure times per layer resulted in the formation of smaller features at the cost of overcure (blurring) of larger ones. The smallest features observed were ∼300, ∼170, and ∼100 μm in diameter at exposure times of 14, 28, and 56 s/25 μm layer, respectively. Surface area analysis revealed good feature fidelity. In other words, the experimental thickness matched the target, with the latter represented by a dashed line in the surface area plot (Figure 4a, right). From these findings, an exposure time of 14 s/25 μm layer (6.5 mm/h) was selected, along with 35 s/100 μm layer (10.3 mm/h), for all future prints to provide a balance between printing speed, feature size, and print fidelity (Table S11).

Vertical resolution, or cure-through, was characterized as a function of CB loading from 0 to 0.1 wt % for small structures with horizontal overhangs, referred to here as bridges (Figure 4b). The bridge prints contained eight bridges, each with an overhang that was designed to be 1000 μm thick (40 × 25 μm layers, Figure S30). Optical profilometry was used to measure the overhang thickness for each print by taking an average across the full width of the overhang on each bridge and averaging those values for all eight bridges to provide the following for 0, 0.01, 0.02, 0.05, and 0.1 wt % CB loading: 1390 ± 100, 1300 ± 46, 1210 ± 83, 1090 ± 78, and 1060 ± 100 μm, respectively (Figure 4b, Figure S31−34, and Table S12). Thus, as the amount of CB increased, the cure-through (z-overcure) decreased, with 0.1 wt % providing the optimal loading. Attempts to use >0.1 wt % CB loading were unsuccessful, which was attributed to the shallow light penetration depth.

To highlight the unique applicability of NIR light 3D printing, we introduced nanoparticle fillers into the optimized resins to prepare high-resolution composite objects. The effects of incident wavelength (405 vs 850 nm), particle composition, and particle loading on light attenuation and concomitant overcure were characterized. Two different nanoparticles, silica (SiO_2, 200 nm diameter) and zirconia (ZrO_2, dispersed with 3 mol% yittria (Y_2O_3), 40 nm diameter), were selected for their utility in glass and ceramic manufacturing,[51] respectively, along with their disparate refractive index (n) values that directly relate to the light scattering intensity in the Rayleigh regime. Specifically, SiO_2 has an $n \approx 1.47$[52] and ZrO_2 an $n \approx 2.16$.[53] To create a homogeneous nanoparticle suspension, SiO_2 and ZrO_2 were ultrasonicated in HDDA:PETMP (95:5), with a surfactant (DispersBYK-180) added to aid in the suspension of ZrO_2. Light attenuation was characterized using thin film (25 and 100 μm) UV−vis absorption spectroscopy and converted to transmittance (Figure 5a and Figures S35−S37). Little-to-no

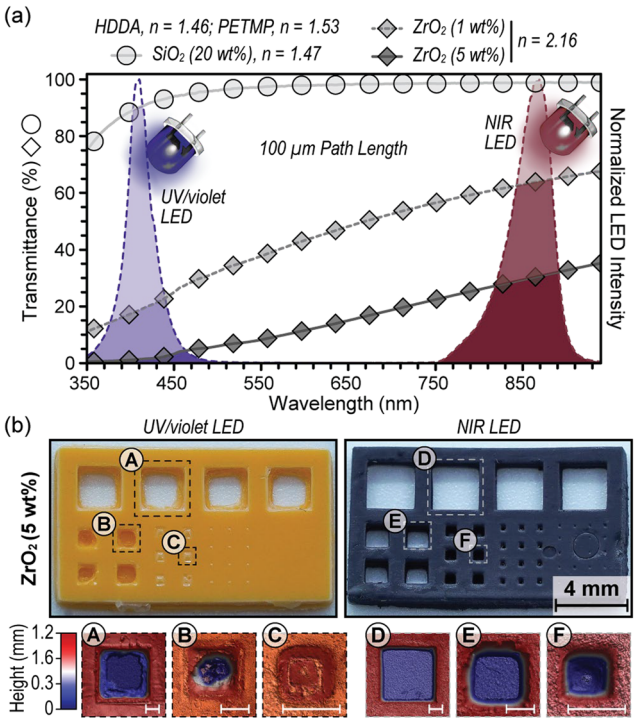

Figure 5. Analysis of nanoparticle resins and 3D printed structures therefrom. (a) Transmittance of 100 μm thick films comprised of HDDA:PETMP (95:5) and SiO_2 (∼200 nm diameter) or ZrO_2 (∼40 nm diameter) at different loadings. For legibility, symbols present on the transmittance curves represent one in every 50 data points collected. (b) Representative photographs of 3D printed structures having different hole sizes to determine the effect of light wavelength used for fabrication and nanoparticle composition on lateral resolution. Expanded images on the bottom are topographical maps collected using optical profilometry for the labeled sections.

attenuation of UV-to-NIR light (∼350−950 nm) was observed for SiO_2 particles at all loadings tested from 1 to 20 wt % (relative to monomer). In contrast, ZrO_2 particles provided intense scattering at low loadings of 1 and 5 wt %, despite their smaller size compared to the SiO_2 particles (confirmed by dynamic light scattering, Figures S38 and S39). Specifically, at ∼405 nm, the transmittance was ∼90%, 18%, and 1% for SiO_2 (20 wt %) and ZrO_2 (1 and 5 wt %), respectively. At ∼850 nm, the transmittance was ∼99, 63, and 29% for SiO_2 (20 wt %)

https://doi.org/10.1021/acsami.1c22046
ACS Appl. Mater. Interfaces XXXX, XXX, XXX−XXX

and ZrO_2 (1 and 5 wt %), respectively. This unambiguous difference in light attenuation for SiO_2 and ZrO_2 is directly attributed to the near match in n for SiO_2 relative to HDDA ($n \approx 1.46$)[54] as the main resin constituent (with PETMP similar at $n \approx 1.53$).[55]

A custom digital file with square hole arrays of varying sizes from 128 (= 2688 μm) to 8 (= 168 μm) pixels wide was used to examine the effect of wavelength on lateral curing resolution for optimized resins containing SiO_2 and ZrO_2 nanoparticles (Figure 5b and Figure S47). Composite printing was accomplished (100 μm layers) using UV−violet (405 nm) light for Type I resins containing BAPO and Sudan I as the opaquing agent and NIR (850 nm) light for Type II resins containing the three-component photosystem and 0.1 wt % CB (see section 3.6 for further details). It was immediately apparent by eye that prints prepared with ZrO_2 nanoparticles and shorter-wavelength UV−violet light resulted in a greater extent of overcure (smaller square holes) relative to those prepared without ZrO_2 nanoparticles or with SiO_2 nanoparticles and NIR light. Optical profilometry was used to quantify the extent of overcure by measuring the volume within each square and dividing it by the digital input parameters based on the final height of the postcured objects (~1 mm). Taking the 32 × 32 pixels as a representative case, the prints prepared with 5 wt % ZrO_2 resulted in near quantitative closure of the square holes using UV−violet light (Figure 5b, image C) and nearly 50% of the hole volume remained using NIR light (Figure 5b, image F). However, it was also observed that more overcure was present for the UV−violet light prints relative to the NIR light prints in the absence of nanoparticles (see Figures S48−S72). This is hypothesized to arise from factors other than scattering, such as thermal overcure. As such, further experiments are necessary to systematically deconvolute the relative contributions of different factors (e.g., scattering and heat) on 3D printing fidelity.

CONCLUDING REMARKS

A highly efficient three-component photosystem for rapid photocuring (<60 s) using a low-intensity (<5 mW/cm^2) NIR LED ($\lambda \approx 850$ nm) was identified, characterized, and implemented in digital light processing 3D printing. The combination of an NIR absorbing cyanine dye, butyltriphenylborate electron donor, and diphenyliodonium electron acceptor facilitated photoredox catalysis for fast acrylate polymerizations. These polymerizations could be performed with low photocatalyst loadings (0.1 mol % H-Nu 815) under ambient (room temperature and air) conditions with the addition of thiol. Real-time monitoring with photoFTIR and photorheology under 3D printing relevant conditions (wavelength, light intensity, and sample thickness) revealed a monomer conversion rate of ~3%/s and a gel point of <30 s. Translation to NIR 3D printing was accomplished by optimizing exposure time per layer and introducing carbon black (CB) as an opaquing agent to balance print speed and feature resolution. Ultimately, the inclusion of CB-enabled features as small as ~100 μm (lateral, x,y-dimension) and 25 μm (vertical, z-dimension) to be achieved with exposure times of <60 s/layer. Furthermore, structures with larger lateral features (≳300) could be printed at an exposure time of 35 s/100 μm layer, providing a rate of ~10 mm/h. Finally, as a proof-of-concept, composite 3D prints containing high-refractive-index ZrO_2 nanoparticles that intensely scatter light were accomplished with improved feature fidelity when using NIR light relative to UV−violet light. This provided preliminary evidence that NIR light-based 3D printing may facilitate the fabrication of detailed composite objects, where high refractive index materials can benefit optoelectronics applications and provide excellent wear and chemical resistance for high-performance bearings and dental implants. Building from the present work, ongoing research efforts include (1) improving photocatalyst design for even faster NIR curing (<10 s/100 μm layer), (2) identifying NIR light-activated resin compositions with longer shelf life stability (approximately months), (3) systematically correlating wavelength-to-resolution for composite 3D printing, and (4) identifying UV−visible−NIR photosystem combinations that enable wavelength-selective fabrication for the preparation of multifunctional 3D objects.

EXPERIMENTAL SECTION

Materials. All chemicals were used as received unless otherwise noted. 2-[2-[2-Chloro-3-[2-(1,3-dihydro-1,1,3-trimethyl2H-benzo[e]-indol-2-ylidene)-ethylidene]-1-cyclohexen-1-yl]-ethenyl]-1,1,3-trimethyl 1Hbenzo[e]indolium, butyltriphenylborate (H-Nu 815), [4-(octyloxy)phenyl](phenyl)iodonium hexafluoroantimonate diphenyliodonium (H-Nu 254), and 2-(butyryloxy)-*N*,*N*,*N*-trimethylethan-1-aminium butyltriphenylborate (Borate V) were purchased/supplied from Spectra Photopolymers. Acetylene carbon black (100% compressed, 42 nm diameter) was purchased from Strem Chemicals, Inc. Pentaerythritol tetrakis(3-mercaptopropionate) (PETMP, >95%), (2,2,6,6-tetramethylpiperidin-1-yl)oxidanyl (TEMPO, 98%), and octadecanoic (stearic) acid (SA, 95%) were purchased from Sigma-Aldrich. 1,6-Hexanediol diacrylate (HDDA, 99%) was purchased from Tokyo Chemical Industry. Silicon dioxide (silica, SiO_2) (spherical, 200 nm) was purchased from U.S. Research Nanomaterials, Inc. Zirconium dioxide (zirconia, ZrO_2) (3 mol % yttrium oxide, 40 nm) was purchased from Tosoh Corporation. DisperBYK-180 (surfactant) was supplied by BYK USA. Note that monomers and cross-linkers were not purified prior to use, and as such any inhibitor present (e.g., phenolics) from the commercial source remained. Chemical structures are provided in Figure S1.

Sample Preparation. *Standard Resin Formulation.* Representative resin formulations are summarized in Table S1. Samples were formulated in the dark to avoid the onset of polymerization. TEMPO (0.005 mol %) was added to HDDA and PETMP, respectively, to serve as stock solutions for resin preparation. The HDDA stock solution was stored in the fridge and was allowed to return to room temperature prior to weighing. HDDA and PETMP stock solutions were first added, and then the other components of the photosystem, with H-Nu 815 added last, and mixed with a 130 W ultrasonicator (Fisherbrand FS60D) at 40 kHz for 5 min. Composite resin formulation: Representative resin formulations are summarized in Table S1. Samples were formulated in the dark to avoid onset of polymerization. TEMPO (0.005 mol %) was added to HDDA and PETMP, respectively, to serve as stock solutions for resin preparation. The HDDA stock solution was stored in the fridge and was allowed to return to room temperature prior to weighing. HDDA and PETMP stock solutions were first added, followed by the addition of nanoparticle(s) and surfactants (stearic acid for carbon black and/or DispersBYK-180 for zirconia). The samples were then mixed with a 500 W ultrasonic processor (part no. VC 505A, Sonics & Materials) for 20 s at a 40% amplitude setting using a 13 mm (0.5 in.) diameter and 139 mm (5.5 in.) solid Ti_6Al_4V titanium alloy probe (part no. 630−0219, Sonics & Materials) within a sound enclosure containing a support rod and converter clamp (part no. 830-00427, Sonics & Materials). Subsequently, the other components of the photosystem were added to the vessel, with H-Nu 815 added last, and mixed with a 130 W ultrasonicator (Fisherbrand FS60D) at 40 kHz for 5 min.

Light Sources. For FTIR spectroscopy and photorheology experiments, NIR light was provided by a Type A LED (serial no.

https://doi.org/10.1021/acsami.1c22046
ACS Appl. Mater. Interfaces XXXX, XXX, XXX−XXX

LCS-0850-03-22, Mightex Systems) with an emission centered at 850 nm and UV−violet light was provided by a Type B LED (serial no. LCS-0405-12-22, Mightex Systems) with an emission centered at 405 nm. These LEDs were used in combination with a current-adjustable driver (SLC-MA02-U, Mightex Systems) for intensity control, such that all intensities between experiments (printing, FTIR, and photorheology) could be matched as accurately as possible. Irradiation intensities were measured with a Thorlabs PM100D photometer equipped with a silicon-based photodiode power sensor (S120VC, Thorlabs). Emission profiles were recorded with a QE pro spectrometer, in which the LED was connected to the fiber optic system using a 3 mm liquid lightguide from Mightex Systems (serial no. LLG-03-59-340-0800-1). See the 3D printing section for additional details, including light intensity.

UV−Vis Absorption Spectroscopy. Light attenuation was measured using UV−visible absorption spectroscopy for all resin formulations and resin components by sandwiching the liquid between two glass slides (cat. no. 12-550-A3, Fisher Scientific) separated by spacers (color-coded shim stock, polyester plastic, McMaster-Carr) with variable thicknesses (25−100 μm). Each sample was placed on a horizontal transmission accessory (Stage RTL-T, Ocean Insight) connected to a spectrometer (QE PRO-ABS, Ocean Insight) through QP-600-025-SR optical fibers. A deuterium-tungsten halogen light source (DH-2000-BAL, Ocean Insight) was used as the probe light. Spectra were collected from 200 to 800 nm; however, data below 350 nm were not analyzed because of attenuation from glass. Extinction coefficients were calculated using Beer's law.

Fourier Transform Infrared Spectroscopy (photoFTIR). Resin formulations were introduced between two 1 mm thick glass microscope slides (cat. no. 12-550-A3, Fisher Scientific) separated by ∼100 μm polyester plastic shims (cat. no. 9513K66, McMaster-Carr) to maintain a constant sample thickness over the course of the photopolymerization. Each sample was placed in a horizontal transmission accessory (A043-N/Q, Bruker) equipped on the FTIR spectrometer (INVENIO-R, Bruker), which was controlled using OPUS spectroscopy software. Spectra were collected from 2000 to 7000 cm^{-1} at a rate of 1 scan every 0.36 s. Most samples were monitored under ambient conditions (atmospheric and room temperature and pressure). The functional group conversion upon light exposure was determined by monitoring the disappearance of the peak area centered at ∼3100 cm^{-1} corresponding to the C═C stretch and ∼2570 cm^{-1} corresponding to the S−H stretch.[46,47] Each sample was tested in triplicate and at printer light intensities (4.6 mW/cm^2 for 850 nm LED and 8.8 mW/cm^2 for 405 nm LED).

Photorheology. Photorheology experiments were completed using a Discovery hybrid rheometer from TA Instruments (TA Instruments, DE, USA). The rheometer was equipped with a "UV Light Guide" accessory, a disposable 20 mm diameter acrylic bottom plate, and a 20 mm diameter geometry aluminum upper parallel plate. A liquid light guide was used to illuminate the samples with the corresponding visible light using an 850 nm LED connected to a driver from which light intensity could be controlled remotely through software. Each sample was tested six times at the printer light intensity (4.6 mW/cm^2 for 850 nm). The rheometer was set to run for three data acquisition cycles with the following experimental parameters: (1) conditioning (axial force = 0 N), (2) dynamic time sweep at 1% strain (60 s), (3) fast oscillation step at 1% strain (50 s), (4) dynamic time sweep at 1% strain (60 s). The gap height was set to 100 μm for each experiment to best match the photoFTIR spectroscopy experiments. Photorheology was performed under ambient conditions (no argon degassing and open to air) for all samples. The light was not turned on until 10 s into the fast oscillation step (step 3). The storage modulus (G') and the loss modulus (G'') were monitored in real time and the light was turned off following inflection of the data, as noted by eye. To determine the gel point (where storage and loss modulus cross), we averaged the fast oscillation step G' and G'' for each trial and plotted as a function of time. The observed time point at which the moduli crossed or changed in concavity was taken to be the point of gelation from when the light was turned on.

3D Printing. 3D printing was performed using a custom-made, DLP-based 3D printer (Monoprinter, MA, USA). Detailed information about the 3D printer can be found in our previous report.[17] A near-infrared (NIR) LED was used as the irradiation source (product no. CBM-90-IRD, Luminus) for projection in the present work. See Figure S2 for the diagram of the LED chips for each printer light source. The full width at half-maximum (fwhm) of the printer NIR LED is 51 nm, with a peak wavelength of 869 nm, whereas the fwhm for the NIR LED used for photoFTIR and photorheology measurements is 29 nm with a peak wavelength of 855 nm. These differences may account for some of the subtle differences observed between printing and photocuring kinetics. The projector resolution was 1920 × 1080 pixels, with each pixel being ∼21 μm × 21 μm at the image plane. The minimum achievable layer thickness is 25 μm. Here, prints were performed using a layer thickness of 25 or 100 μm, which is noted in the figure caption. Printing parameters (base exposure time and normal layer exposure time) can also be found in figure captions of printed objects. Upon completion of each print, the resultant objects were rinsed with acetone, air-dried, and postcured with UV light centered at 370 nm (part no. ANYCUBIC-WASH-CURE) for 20 min.

Optical Profilometry. A laser scanning optical 3D microscope (VK-X1100, Keyence) was used to map the topography of each print. Multifile analyzer software (Keyence) was used to calculate the height, surface area, and volume for different prints. For clarity, the specific measurement details are found in the Characterization section of the Supporting Information.

Dynamic Light Scattering. A dynamic light scattering instrument (Zetasizer Nano ZS) was used to determine the particle size (diameter, nm) of nanoparticles dispersed in the resin. Nanoparticles were prepared by suspension in 95:5 HDDA:PETMP (molar equivalents) mixture via ultrasonification. Samples were immediately transported to the Zetasizer instrument and size measurements were performed using a refractive index value of 1.46 for HDDA as the primary dispersant, 1.47 for SiO_2 nanoparticles, and 2.16 for ZrO_2 nanoparticles. Samples were placed in quartz cuvettes and allowed to equilibrate in the instrument up to room temperature (25 °C) for 120 bs. The angle of measurement used was 173° backscattered for all measurements. Data were compiled and analyzed using the Malvern Zetasizer software version 7.13.

Tensile Testing. Mechanical samples were printed as dogbones with the following dimensions: 0.75 mm (thickness), 1.17 mm (gauge width), and 12.3 mm (gauge length). Prints were accomplished with various resins as noted in the text, and postcured with UV light centered at 370 nm (part no. ANYCUBIC-WASH-CURE) for 20 min. Uniaxial tension was applied to each sample under ambient conditions using a tensile tester (AGS-500NXD, SHIMADZU) equipped with a load cell (1 kN capacity) at a crosshead speed of 2 mm/min (strain rate of 16.3%/min). Experiments were repeated at least five times for each sample and the displayed results represent an average ± one standard deviation of all runs.

■ ASSOCIATED CONTENT

Supporting Information

The Supporting Information is available free of charge at https://pubs.acs.org/doi/10.1021/acsami.1c22046.

Additional experimental and instrumentation details and characterization, including thin film absorption, LED emission, photocuring kinetics, 3D printing optimization, images of 3D prints, mechanical properties of prints, and the effects of carbon black, surfactant, and nanoparticles on photocuring and 3D printing (PDF)

https://doi.org/10.1021/acsami.1c22046
ACS Appl. Mater. Interfaces XXXX, XXX, XXX−XXX

AUTHOR INFORMATION

Corresponding Author

Zachariah A. Page − *Department of Chemistry, The University of Texas at Austin, Austin, Texas 78712, United States;* orcid.org/0000-0002-1013-5422; Email: zpage@utexas.edu

Authors

Lynn M. Stevens − *Department of Chemistry, The University of Texas at Austin, Austin, Texas 78712, United States;* orcid.org/0000-0002-7956-8277

Clotilde Tagnon − *Department of Chemistry, The University of Texas at Austin, Austin, Texas 78712, United States;* orcid.org/0000-0002-6544-5620

Complete contact information is available at: https://pubs.acs.org/10.1021/acsami.1c22046

Notes

The authors declare no competing financial interest.

ACKNOWLEDGMENTS

We thank the Robert A. Welch Foundation (F-2007) for financial support. The authors acknowledge the use of shared research facilities supported in part by the Texas Materials Institute, the Center for Dynamics and Control of Materials: an NSF MRSEC (DMR-1720595), and the NSF National Nanotechnology Coordinated Infrastructure (ECCS-1542159). We thank Spectra Photopolymers for their in-kind support with supplying the Borate V and H-Nu 254 used in this study and Dr. Yun-Ho Jang at MonoPrinter for support with the custom DLP 3D printer and software design.

ABBREVIATIONS

DLP, digital light processing; LCD, liquid crystal display; UV, ultraviolet; NIR, near-infrared; LED, light emitting diode; PI, photoinitiator; PRC, photoredox catalyst; D, electron donor; A, electron acceptor; FTIR, Fourier transform infrared; BAPO, bis-acylphosphine oxide; HDDA, 1,6-hexanediol diacrylate; PETMP, pentaerythritol tetrakis(3-mercaptopropionate); CB, carbon black

REFERENCES

(1) Bagheri, A.; Jin, J. Photopolymerization in 3D Printing. *ACS Appl. Polym. Mater.* **2019**, *1* (4), 593−611.

(2) Jung, K.; Corrigan, N.; Ciftci, M.; Xu, J.; Seo, S. E.; Hawker, C. J.; Boyer, C. Designing with Light: Advanced 2D, 3D, and 4D Materials. *Adv. Mater.* **2020**, *32*, 1903850.

(3) Truby, R. L.; Lewis, J. A. Printing Soft Matter in Three Dimensions. *Nature* **2016**, *540* (7633), 371−378.

(4) Zhang, J.; Xiao, P. 3D Printing of Photopolymers. *Polym. Chem.* **2018**, *9* (13), 1530−1540.

(5) Narupai, B.; Nelson, A. 100th Anniversary of Macromolecular Science Viewpoint: Macromolecular Materials for Additive Manufacturing. *ACS Macro Lett.* **2020**, *9* (5), 627−638.

(6) Sampson, K. L.; Deore, B.; Go, A.; Nayak, M. A.; Orth, A.; Gallerneault, M.; Malenfant, P. R. L.; Paquet, C. Multimaterial Vat Polymerization Additive Manufacturing. *ACS Appl. Polym. Mater.* **2021**, *3* (9), 4304−4324.

(7) Wallin, T. J.; Pikul, J.; Shepherd, R. F. 3D Printing of Soft Robotic Systems. *Nat. Rev. Mater.* **2018**, *3* (6), 84−100.

(8) Lu, P.; Ahn, D.; Yunis, R.; Delafresnaye, L.; Corrigan, N.; Boyer, C.; Barner-Kowollik, C.; Page, Z. A. Wavelength-Selective Light-Matter Interactions in Polymer Science. *Matter* **2021**, *4* (7), 2172−2229.

(9) Tumbleston, J. R.; Shirvanyants, D.; Ermoshkin, N.; Janusziewicz, R.; Johnson, A. R.; Kelly, D.; Chen, K.; Pinschmidt, R.; Rolland, J. P.; Ermoshkin, A.; Samulski, E. T.; DeSimone, J. M. Continuous Liquid Interface Production of 3D Objects. *Science.* **2015**, *347* (6228), 1349−1352.

(10) Walker, D. A.; Hedrick, J. L.; Mirkin, C. A. Rapid, Large-Volume, Thermally Controlled 3D Printing Using a Mobile Liquid Interface. *Science.* **2019**, *366* (6463), 360−364.

(11) Xiao, P.; Zhang, J.; Dumur, F.; Tehfe, M. A.; Morlet-Savary, F.; Graff, B.; Gigmes, D.; Fouassier, J. P.; Lalevée, J. Visible Light Sensitive Photoinitiating Systems: Recent Progress in Cationic and Radical Photopolymerization Reactions under Soft Conditions. *Prog. Polym. Sci.* **2015**, *41*, 32−66.

(12) Schwartz, J. J.; Boydston, A. J. Multimaterial Actinic Spatial Control 3D and 4D Printing. *Nat. Commun.* **2019**, *10* (1), 791.

(13) Dumur, F. Recent Advances on Visible Light Metal-Based Photocatalysts for Polymerization under Low Light Intensity. *Catalysts* **2019**, *9*, 736.

(14) Zakeri, S.; Vippola, M.; Levänen, E. A Comprehensive Review of the Photopolymerization of Ceramic Resins Used in Stereolithography. *Addit. Manuf.* **2020**, *35*, 101177.

(15) Yu, C.; Schimelman, J.; Wang, P.; Miller, K. L.; Ma, X.; You, S.; Guan, J.; Sun, B.; Zhu, W.; Chen, S. Photopolymerizable Biomaterials and Light-Based 3D Printing Strategies for Biomedical Applications. *Chem. Rev.* **2020**, *120*, 10695−10743.

(16) Nieto, D.; Marchal Corrales, J. A.; Jorge de Mora, A.; Moroni, L. Fundamentals of Light-Cell − Polymer Interactions in Photo-Cross-Linking Based Bioprinting Fundamentals of Light-Cell − Polymer Interactions in Photo-Cross-Linking Based Bioprinting. *APL Bioeng.* **2020**, *4*, 041502.

(17) Ahn, D.; Stevens, L. M.; Zhou, K.; Page, Z. A. Rapid High-Resolution Visible Light 3D Printing. *ACS Cent. Sci.* **2020**, *6* (9), 1555−1563.

(18) Stafford, A.; Ahn, D.; Raulerson, E. K.; Chung, K.-Y.; Sun, K.; Cadena, D. M.; Forrister, E. M.; Yost, S. R.; Roberts, S. T.; Page, Z. A. Catalyst Halogenation Enables Rapid and Efficient Polymerizations with Visible to Far-Red Light. *J. Am. Chem. Soc.* **2020**, *142* (34), 14733−14742.

(19) Ahn, D.; Stevens, L. M.; Zhou, K.; Page, Z. A. Additives for Ambient 3D Printing with Visible Light. *Adv. Mater.* **2021**, *33*, 2104906.

(20) Seo, S. E.; Kwon, Y.; Dolinski, N. D.; Sample, C. S.; Self, J. L.; Bates, C. M.; Valentine, M. T.; Hawker, C. J. Three-Dimensional Photochemical Printing of Thermally Activated Polymer Foams. *ACS Appl. Polym. Mater.* **2021**, *3*, 4984−4991.

(21) Zhu, G.; Hou, Y.; Xiang, J.; Xu, J.; Zhao, N. Digital Light Processing 3D Printing of Healable and Recyclable Polymers with Tailorable Mechanical Properties. *ACS Appl. Mater. Interfaces* **2021**, *13* (29), 34954−34961.

(22) Zhang, Z.; Corrigan, N.; Bagheri, A.; Jin, J.; Boyer, C. A Versatile 3D and 4D Printing System through Photocontrolled RAFT Polymerization. *Angew. Chemie - Int. Ed.* **2019**, *58* (50), 17954−17963.

(23) Li, W.; Wang, M.; Mille, L. S.; Robledo Lara, J. A.; Huerta, V.; Uribe Velázquez, T.; Cheng, F.; Li, H.; Gong, J.; Ching, T.; Murphy, C. A.; Lesha, A.; Hassan, S.; Woodfield, T. B. F.; Lim, K. S.; Zhang, Y. S. A Smartphone-Enabled Portable Digital Light Processing 3D Printer. *Adv. Mater.* **2021**, *33*, 2102153.

(24) Xu, X.; Seijo-Rabina, A.; Awad, A.; Rial, C.; Gaisford, S.; Basit, A. W.; Goyanes, A. Smartphone-Enabled 3D Printing of Medicines. *Int. J. Pharm.* **2021**, *609*, 121199.

(25) Liu, R.; Chen, H.; Li, Z.; Shi, F.; Liu, X. Extremely Deep Photopolymerization Using Upconversion Particles as Internal Lamps. *Polym. Chem.* **2016**, *7* (14), 2457−2463.

(26) Zhu, J.; Zhang, Q.; Yang, T.; Liu, Y.; Liu, R. 3D Printing of Multi-Scalable Structures via High Penetration near-Infrared Photopolymerization. *Nat. Commun.* **2020**, *11*, 3462.

(27) Strehmel, B.; Schmitz, C.; Kütahya, C.; Pang, Y.; Drewitz, A.; Mustroph, H. Photophysics and Photochemistry of NIR Absorbers

Derived from Cyanines: Key to New Technologies Based on Chemistry 4.0. *Beilstein J. Org. Chem.* **2020**, *16*, 415−444.
(28) Schmitz, C.; Pang, Y.; Gülz, A.; Gläser, M.; Horst, J.; Jäger, M.; Strehmel, B. New High-Power LEDs Open Photochemistry for Near-Infrared- Sensitized Radical and Cationic Photopolymerization. *Angew. Chem.* **2019**, *131* (13), 4445−4450.
(29) Strehmel, B.; Schmitz, C.; Cremanns, K.; Göttert, J. Photochemistry with Cyanines in the Near Infrared: A Step to Chemistry 4.0 Technologies. *Chem. - A Eur. J.* **2019**, *25* (56), 12855−12864.
(30) Siebrand, W. Radiationless Transitions in Polyatomic Molecules. II. Triplet-Ground-State Transitions in Aromatic Hydrocarbons. *J. Chem. Phys.* **1967**, *47* (7), 2411−2422.
(31) Englman, R.; Jortner, J. The Energy Gap Law for Radiationless Transitions in Large Molecules. *Mol. Phys.* **1970**, *18* (2), 145.
(32) Pang, Y.; Shiraishi, A.; Keil, D.; Popov, S.; Strehmel, V.; Jiao, H.; Gutmann, J. S.; Zou, Y.; Strehmel, B. NIR-Sensitized Cationic and Hybrid Radical/Cationic Polymerization and Crosslinking. *Angew. Chemie - Int. Ed.* **2021**, *60* (3), 1465−1473.
(33) Pang, Y.; Jiao, H.; Zou, Y.; Strehmel, B. The NIR-Sensitized Cationic Photopolymerization of Oxetanes in Combination with Epoxide and Acrylate Monomers. *Polym. Chem.* **2021**, *12* (40), 5752−5759.
(34) Schmitz, C.; Halbhuber, A.; Keil, D.; Strehmel, B. NIR-Sensitized Photoinitiated Radical Polymerization and Proton Generation with Cyanines and LED Arrays. *Prog. Org. Coatings* **2016**, *100*, 32−46.
(35) Pang, Y.; Fan, S.; Wang, Q.; Oprych, D.; Feilen, A.; Reiner, K.; Keil, D.; Slominsky, Y. L.; Popov, S.; Zou, Y.; Strehmel, B. NIR-Sensitized Activated Photoreaction between Cyanines and Oxime Esters: Free-Radical Photopolymerization. *Angew. Chemie - Int. Ed.* **2020**, *59* (28), 11440−11447.
(36) Bonardi, A. H.; Dumur, F.; Grant, T. M.; Noirbent, G.; Gigmes, D.; Lessard, B. H.; Fouassier, J. P.; Lalevée, J. High Performance Near-Infrared (NIR) Photoinitiating Systems Operating under Low Light Intensity and in the Presence of Oxygen. *Macromolecules* **2018**, *51* (4), 1314−1324.
(37) Bonardi, A.; Bonardi, F.; Noirbent, G.; Dumur, F.; Dietlin, C.; Gigmes, D.; Fouassier, J. P.; Lalevée, J. Different NIR Dye Scaffolds for Polymerization Reactions under NIR Light. *Polym. Chem.* **2019**, *10* (47), 6505−6514.
(38) Mokbel, H.; Noirbent, G.; Gigmes, D.; Dumur, F.; Lalevée, J. Towards New NIR Dyes for Free Radical Photopolymerization Processes. *Beilstein J. Org. Chem.* **2021**, *17*, 2067−2076.
(39) Elim, H. I.; Cai, B.; Sugihara, O.; Kaino, T.; Adschiri, T. Rayleigh Scattering Study and Particle Density Determination of a High Refractive Index TiO2 Nanohybrid Polymer. *Phys. Chem. Chem. Phys.* **2011**, *13* (10), 4470−4475.
(40) Piazza, R.; Eghan, M. J.; Peyre, V.; Degiorgio, V. Light Scattering Investigation of Amphiphile and Polymer Adsorption on the Surface of Colloidal Particles with Low Optical Contrast. *Prog. Colloid Polym. Sci.* **1998**, *110*, 89−93.
(41) Sims, P. J.; Waggoner, A. S.; Wang, C. H.; Hoffman, J. F. Studies on the Mechanism by Which Cyanine Dyes Measure Membrane Potential in Red Blood Cells and Phosphatidylcholine Vesicles. *Biochemistry* **1974**, *13* (16), 3315−3330.
(42) Spectra Photopolymers. https://www.sglinc.com/ (accessed 2021-11-07).
(43) Polykarpov, A. Y.; Neckers, D. C. Tetramethylammonium Phenyltrialkylborates in the Photoinduced Electron Transfer Reaction with Benzophenone. Generation of Alkyl Radicals and Their Addition to Activated Alkenes. *Tetrahedron Lett.* **1995**, *36* (31), 5483−5486.
(44) Kabatc, J.; Jędrzejewska, B.; Pączkowski, J. Hemicyanine N-Butyltriphenylborate Salts as Effective Initiators of Free-Radical Polymerization Photoinitiated via Photoinduced Electron-Transfer Process. *J. Polym. Sci. Part A Polym. Chem.* **2003**, *41* (19), 3017−3026.
(45) Garra, P.; Dietlin, C.; Morlet-Savary, F.; Dumur, F.; Gigmes, D.; Fouassier, J. P.; Lalevée, J. Redox Two-Component Initiated Free Radical and Cationic Polymerizations: Concepts, Reactions and Applications. *Prog. Polym. Sci.* **2019**, *94*, 33−56.
(46) Chatani, S.; Gong, T.; Earle, B. A.; Podgorski, M.; Bowman, C. N. Visible-Light Initiated Thiol-Michael Addition Photopolymerization Reactions. *ACS Macro Lett.* **2014**, *3* (4), 315−318.
(47) Pretsch, E.; Bühlmann, P.; Badertscher, M. *Structure Determination of Organic Compounds: Tables of Spectral Data*; 4th ed.; Springer, 2009; p 304.
(48) Lee, M. P.; Cooper, G. J. T.; Hinkley, T.; Gibson, G. M.; Padgett, M. J.; Cronin, L. Development of a 3D Printer Using Scanning Projection Stereolithography. *Sci. Rep.* **2015**, *5*, 9875.
(49) Würthner, F.; Kaiser, T. E.; Saha-Möller, C. R. J-Aggregates: From Serendipitous Discovery to Supramolecular Engineering of Functional Dye Materials. *Angew. Chemie - Int. Ed.* **2011**, *50* (15), 3376−3410.
(50) Bricks, J. L.; Slominskii, Y. L.; Panas, I. D.; Demchenko, A. P. Fluorescent J-Aggregates of Cyanine Dyes: Basic Research and Applications Review. *Methods Appl. Fluoresc.* **2018**, *6*, 012001.
(51) He, R.; Liu, W.; Wu, Z.; An, D.; Huang, M.; Wu, H.; Jiang, Q.; Ji, X.; Wu, S.; Xie, Z. Fabrication of Complex-Shaped Zirconia Ceramic Parts via a DLP- Stereolithography-Based 3D Printing Method. *Ceram. Int.* **2018**, *44* (3), 3412−3416.
(52) Silica Glass (SiO2) Optical Material. https://www.crystran.co.uk/optical-materials/silica-glass-sio2 (accessed 2021-11-07).
(53) Wood, D. L.; Nassau, K. Refractive Index of Cubic Zirconia Stabilized with Yttria. *Appl. Opt.* **1982**, *21* (16), 2978.
(54) 1,6-Hexanediol diacrylate technical grade, 80%. https://www.sigmaaldrich.com/US/en/product/aldrich/246816 (accessed 2021-11-07).
(55) Pentaerythritol tetrakis(3-mercaptopropionate), > 95%. https://www.sigmaaldrich.com/US/en/product/aldrich/381462 (accessed 2021-11-07).

https://doi.org/10.1021/acsami.1c22046
ACS Appl. Mater. Interfaces XXXX, XXX, XXX−XXX